Melting behavior of uranium-americium mixed oxides under different atmospheres

E. Epifano, D. Prieur, P. Martin, C. Gueneau, K. Dardennes, J. Rothe, T. Vitova, O. Dieste, T. Wiss, R. J.M. Konings, et al.

HAL Id: cea-02340026

https://cea.hal.science/cea-02340026

Submitted on 5 Nov 2019

Melting behavior of uranium-americium mixed oxides under different atmospheres

E. Epifano[1,2,3], D. Prieur[4,5], P. M. Martin[1], C. Guéneau[6], K. Dardenne[7], J. Rothe[7], T. Vitova[7], O. Dieste[5],

T.Wiss[5], R. J. M. Konings[5], D. Manara[5]

1. CEA, DEN, DMRC, SFMA, LCC, BP 17171, 30207 Bagnols-sur-Cèze, France
2. Department of Radiation Science and Technology, Faculty of Applied Sciences, Delft University of Technology, Delft 2629JB, The Netherlands.
3. Laboratoire d'Etudes des Microstructures, CNRS-ONERA, Chatillon 92322, France.4 - European Commission, Joint Research Centre Karlsruhe, P.O. Box 2340, 76125 Karlsruhe, Germany.
4. Helmholtz Zentrum Dresden Rossendorf (HZDR), Institute of Resource Ecology, P.O. Box 10119, 01314 Dresden, Germany
5. European Commission, Joint Research Centre Karlsruhe, P.O. Box 2340, 76125 Karlsruhe, Germany.
6. DEN-Service de Corrosion et du Comportement des Matériaux dans leur Environnement (SCCME), CEA, Université Paris-Saclay, F-91191 Gif-sur-Yvette, France.
7- Institut fuer Nukleare Entsorgung (INE), Karlsruhe Institute of Technology Campus Nord, Hermann Von Helmholtz Platz 1, Eggenstein-Leopoldshafen, Germany

Abstract

In the context of a comprehensive campaign for the characterisation of minor actinide transmutation fuels, the melting behaviour of mixed uranium-americium dioxides has been experimentally studied for the first time by laser heating, for Am concentrations up to 70 mol % under different types of atmosphere. Extensive post-melting material characterisation were then performed by X-ray absorption spectroscopy and electron microscopy. The melting temperatures observed for the various compositions follow a markedly different trend depending on the experimental atmosphere. Uranium-rich samples melt at temperatures significantly lower (around 2700 K) when they are laser-heated in a strongly oxidising atmosphere (compressed air at 0.3 MPa), compared to the melting points (beyond 3000 K) registered for the same compositions in an inert environment (pressurised Ar). This behaviour has been interpreted on the basis of the strong over-oxidation in air of such samples, leading to lower-melting actual compositions. Thus, the melting temperature trend observed in air is characterised, in the purely pseudo-binary dioxide plane, by an apparent maximum melting temperature around 2850 K for $0.3 < x(AmO_2) < 0.5$. The melting points measured under inert atmosphere uniformly decrease with increasing americium content, displaying an approximately ideal solution behaviour if a melting point around 2400 K is assumed for pure AmO_2. In reality, it will be shown that the (U, Am) dioxide system can only be rigorously described in the ternary U-Am-O diagram, due to the aforementioned over-oxidation effect in air and general departures from the oxygen stoichiometry (Oxygen/Metal ratios ≠ 2.0) that have been highlighted by the X-ray Absorption Spectroscopy results. Finally, to better understand the experimental results, thermodynamic computations based on the CALPHAD method will be show.

Keywords: Uranium americium dioxide, melting, transmutation targets, Calphad.

1. Introduction

A thorough knowledge of the thermodynamic properties of advanced fuels or Minor Actinide Bearing Blankets (MABB), to which minor actinides (MAs) have been incorporated, is essential in order to put into practice the Partition & Transmutation strategy in fast neutron reactors (FNR).

In a heterogeneous transmutation scenario, $(U,Am)O_2$ pellets with Am/(Am+U) ratios up to 20 mol. % are placed in the periphery of the reactor core, where temperatures can reach 1470 K [1]. For the homogenous transmutation strategy, lower americium contents are foreseen (maximum 5 mol.%), but the pellets are distributed in the entire reactor core. In this case, during normal operation, the fuel is subject to high temperatures (> 2300 K) and strong thermal gradients.

For both scenarios, the thermodynamic properties of the U-Am-O system need to be known for the entire temperature range. In particular, the high temperature thermophysical properties, as for example the melting temperature and the thermal conductivity, are key parameters in the design of a reactor core, because they determine the safety margins and the behaviour of the fuel in the reactor. These properties are dramatically affected by the oxygen stoichiometry of the fuel, usually indicated as the oxygen/metal ratio (O/M). Indeed, the actinide dioxides do not generally form stoichiometric compounds, but solid solutions with large oxygen non-stoichiometric domain. To further complicate the situation, the temperature gradient in the fuel pellets causes a redistribution of both oxygen and metal atoms inside the pellet, meanwhile the overall composition changes with the burnup. The prediction of the possible composition changes and the effects on the thermophysical properties under specific temperature and oxygen potential conditions is thus crucial for the safety perspectives.

The melting behaviour of $UO_{2\pm x}$ has been thoroughly studied in the past decades. Congruent melting occurs for an O/M≈2.0 (1.98 according to the assessment by Gueneau *et al*. [2]), whereas the melting temperature largely decreases for any departure from the oxygen stoichiometry. On the contrary, the melting behaviour of AmO_2 is not well established. Only one set of measurements is reported in the literature [3], in which, moreover, largely scattered values were obtained by varying the heating

rate. The highest obtained melting temperature- of about 2385 K- was associated to AmO_2, but the O/Am ratio was not determined after the melting. However, recent CALPHAD assessments [4], [5] showed that americium dioxide does not melt congruently, since a reduction occurs at high temperature, leading to an O/Am ratio below 2.0. For $(U, Am)O_2$ oxides, very few data are available for the melting temperature and these are limited to low Am/(Am+U) ratios (< 20 mol.%) [6]. It should also be noticed, that the high temperature study of these compounds is particularly challenging, due to their very high radioactivity and the limited amount of americium available for laboratory investigations. This explains the aforementioned lack of data in the U-Am-O system.

In this paper, the melting behaviour of mixed $(U,Am)O_{2\pm x}$ oxides is investigated by a laser-heating technique in a large domain of composition, for 0.075 < Am/(Am+U)<0.7. The results of these novel measurements are discussed in the light of the experimental heating-cooling curves, a comprehensive post-melting material characterisation campaign, based on X-ray absorption spectroscopy (XAS) and electron microscopy, and thermodynamic computations based on the CALPHAD method.

2. Methods

2.1 Material Preparation

$U_{1-y}Am_yO_{2\pm x}$ oxides with nominal americium content x = 0.07, 0.10, 0.20, 0.30, 0.50 and 0.70 were synthetized for this study, each one identified herein with the reference indicated in Table 1. The samples were manufactured as form of small pellets (diameter = 5 mm, height between 3 and 5 mm) in the Atalante facility of CEA Marcoule, using the UMACS powder metallurgy process [7]. The conditions of this process (oxygen potentials ≈ -400 kJ/mol^{-1} at T ≈ 1800 K) have proven to be optimized for manufacturing dense and homogeneous pellets from single oxide precursors, such as UO_2 and AmO_2. The ones used in this work were previously presented in [8].

One pellet from each batch was characterized by XRD, thermal ionization mass spectrometry (TIMS) and XAS. TIMS was used to determine the uranium and americium quantities in the oxides and hence

to precisely know the Am/(Am+U) ratio of the samples. XRD was performed on grounded samples using a Bruker D8 Advance diffractometer in θ-θ Bragg Brentano geometry. For all the compositions, the diffraction patterns confirmed the presence of one single fluorite-type phase, indicating that the formation of the solid solution was achieved. The lattice parameters, obtained from the Pawley refinement of the patterns, are reported in Table 1, together with the sample age at the time. The values- once corrected for the time dependent swelling due to the α-decay, are consistent with those of oxides previously manufactured using the UMACS process [9]. XAS was performed on a few mg of powder for the compositions investigated in this work, at the Rossendorf beamline of the ESRF. The L_3 edges of U and Am were probed and the spectra were compared to those obtained on reference materials (UO_2, U_4O_9, U_3O_8, AmO_2 and an oxalate with Am^{3+}). This allowed determining the average oxidation states of U and Am. Then, from the electroneutrality rule, the O/M ratios were calculated. The same methodology is applied in this work on the melted samples and it will be more detailed in the following. The results of the XAS study on the as-sintered oxides is instead published in another work [10].

Reference	Nominal Am/(Am+U)	Measured composition	XRD data	
			a (Å)	Age (days)
Am7	0.07	$U_{0.93}Am_{0.07}O_{2.01}$	5.467(1)	6
Am10	0.10	$U_{0.90}Am_{0.10}O_{2.01}$	5.466(1)	5
Am20	0.20	$U_{0.81}Am_{0.19}O_{2.01}$	5.460(1)	4
Am30	0.30	$U_{0.72}Am_{0.28}O_{2.02}$	5.455(1)	5
Am50	0.50	$U_{0.52}Am_{0.48}O_{1.97}$	5.456(1)	4
Am70	0.70	$U_{0.33}Am_{0.67}O_{1.90}$	5.450(1)	100

Table 1. Characteristics of the materials used in this work.

2.2 Laser Heating

Melting experiments were performed at Joint Research Centre Karlsruhe using a laser-heating technique coupled with fast pyrometry. The experimental set-up and technique were described in detail in previous works [11]–[13]. The main advantages of the laser-heating technique are the short measurement duration and the quasi-containerless conditions. During the experiment, the investigated pellet is held inside an autoclave, supported in a 3-pin mount by graphite screws, and the laser is focused onto a spot smaller than the sample surface, hence only a limited part is melted. The rest of the pellet can be considered as a "self-crucible" and no contamination with foreign surrounding materials occurs.

In the current experiments, the sample under investigation is heated by a 4.5 kW Nd:YAG CW Laser (HLD4506, TRUMPF, Schramberg, Germany). Radiation pyrometers measure the sample radiance L_{ex}. This is the electromagnetic radiation power density per unit surface, wavelength and solid angle emitted by the sample at a given temperature. It is linked to the sample surface temperature T through modified Planck function:

$$L_{ex} = \frac{L_\lambda}{c_1} = \frac{1}{\lambda^5} \cdot \frac{\varepsilon_\lambda(T)}{e^{\frac{c_2}{\lambda \cdot T}} - 1}$$

Equation 1

L_λ being the radiative power, ε_λ the spectral emissivity, $c_1 = 2 \cdot h \cdot c_0^2$ is the first radiation constant and $c_2 = h \cdot c_0 \cdot k_B = 14388$ µm·K is the second radiation constant, c_0 is the speed of light in vacuum, h is Planck's constant, and k_B Boltzmann's constant. The spectral emissivity takes into account the fact that a real body will radiate, at a given wavelength and temperature, only a fraction equal to ε_λ of the power emitted by an ideal blackbody at the same temperature. Therefore, ε_λ takes values comprised between 0 and 1, 1 corresponding to the ideal blackbody case, for which Planck's law was derived. Since pyrometers in the present work were always set up near normal with respect to the sample surface, the angle dependence of ε_λ was not considered, and 'emissivity' will always refer to normal spectral emissivity (NSE). The NSE must be determined in order to convert, through equation 1 and a pyrometer calibration procedure, L_{ex} into absolute temperature T. The specimen temperature is

detected using a fast pyrometer calibrated against standard lamps up to 2500 K at λ = 655 nm. An additional, 256-channel radiance spectro-pyrometer operating between 515 nm and 980 nm was employed for the study of the sample's NSE (ε_λ). Determination of the NSE is possible by doing a non-linear fit of the thermal emission spectrum with Equation 1 [14], T and ε_λ being the only two free parameters. This approach has been demonstrated to be acceptably accurate in refractory materials [15], like those usually present in a NPPs, for which the NSE can be assumed to be wavelength-independent (grey body hypothesis) on a broad spectral range. For the present oxides, the constant value 0.825 was established for the NSE at the pyrometers' wavelengths, in agreement with previous studies and recent theoretical assessments [16].

Once the temperature of the laser-heated sample is correctly measured as a function of time, thermal analysis can be performed on the resulting temperature-time curve (thermogram). Inflections or thermal arrests in the thermograms give information related to phase transitions (solidus, liquidus and isothermal phase transformations). An additional technique called reflected light signal (RLS) analysis [11] is used to confirm phase transitions. It is conducted by using the second channel of the pyrometer tuned to a low-power (1W) Ar$^+$ laser (λ = 488 nm). This channel detects the laser beam originating from the Ar$^+$ cavity and reflected by the sample surface. A constant RLS signal indicates a solid surface while random oscillations appear after melting due to surface tension-induced vibrations on the sample liquid surface.

Taking into account the instrumental uncertainties linked to the pyrometers' calibration procedures, the uncertainties in the NSE and the experimental data repeatability, the transition temperatures measured in this work are affected by a total relative uncertainty of approximately ±1%, for one standard deviation.

2.3 Electron Microscopy

The SEM observations were performed on a Philips XL40 SEM (Philips, Amsterdam, Netherlands), which has been adapted for the examination of highly active or irradiated nuclear materials: the high voltage unit, column, chamber and turbomolecular pump are mounted inside a glove-box in order to

keep the contaminated pieces in a confined space. The primary vacuum system, water cooling circuit and acquisition electronic are placed outside, preventing those parts from contamination by the active samples. The microscope is equipped with Secondary electrons detector (SE) which gives a morphology-related signal and Backscattered electrons detector (BSE) which provides images with Z-related contrast; the beam was always operated at 20 kV.

2.4 XAS

Small amounts (1-2 mg) of powder were scratched from the melted part of the samples and these were mixed with polyethylene and pressed into pellets. These samples were put in polyethylene sample holders and confined in a double sealed vinyl bag, for measurement at the INE beamline [17] of the KIT Synchrotron light source (Germany), under dedicated operating conditions (2.5 GeV, 120-150 mA). Spectra were collected at the $U-L_3$ and $Am-L_3$ edges (17166, 18510 eV), at room temperatures. Spectra were acquired both in transmission and fluorescence modes, using argon-filled ionization chambers and a Canberra LEGe five pixel fluorescence detector. A Ge(422) double crystal monochromator coupled with collimating and focusing Rh-coated mirrors were used for energy selection. The calibration was performed using metallic foils whose K edges are close to the edges of interest: yttrium (17038 eV), zirconium (17998 eV), and molybdenum (20000 eV). The references were measured at the same time of the samples, in transmission mode.

The X-ray fluorescence emission was used to determine the Am/(Am+U) ratio in the melted samples. The fluorescence intensity I_f is proportional to:

$$I_f \propto \mu(E) \cdot I_0$$

Where I_0 is the is the X-ray intensity incident on the sample and $\mu(E)$ is the absorption coefficient. For incident X-ray with energy E sufficiently far from the absorption edge, $\mu(E)$ is a smooth function of the energy and it can be expressed as:

$$\mu(E) \approx \frac{\rho \, Z^4}{A \, E^3}$$

Equation 2

where *Z* and *A* are respectively the atomic and mass numbers and ρ is the element density. In this case, an excitation energy of E = 18900 eV was used. This energy was chosen because it is beyond the U-L_3 (~ 17166 eV) and Am-L_3 (~ 18510 eV) edges, but below the L_2 edges. Two characteristic fluorescent peaks are observed at about 13614 eV and 14620 eV. The first peak corresponds to the fluoresce X-rays emitted by uranium during the $L_{\alpha 1}$ ($M_5 \rightarrow L_3$) and $L_{\alpha 2}$ ($M_4 \rightarrow L_3$) electronic transitions. The second peak is due to the emissions from americium, for the same electronic transitions $L_{\alpha 1}$ and $L_{\alpha 2}$. Therefore, the ratio between the mass of uranium and americium in the samples was obtained as:
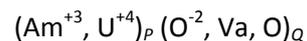
$$\frac{I_f(U)}{I_f(Am)} \propto \frac{m(U)}{m(Am)}$$

Equation 3

The XANES data were analysed using the Athena software [18]. The spectra were normalized using a linear function for pre-edge and post-edge signals. The first zero crossings of the first and second derivatives were used to determine the white line (WL) and the inflection point (E_0), respectively. The average oxidation states of the cations were determined fitting the XANES data by linear combination of reference spectra. UO_2, U_3O_8 and the as-sintered Am30 sample were used for the U-L_3 edge, whereas AmO_2 and Am^{3+}-oxalate were used for the Am-L_3.

2.5 Thermodynamic modelling and computations

Thermodynamic modelling and computations were performed according to the Calphad method. The Am-U-O model from [19] was here adopted as starting point. In [19], in analogy with all the other actinide oxide systems [2], a partially ionic two sublattice liquid model [20] was adopted for the U-Am-O system, with the form:

$$(Am^{+3}, U^{+4})_P (O^{-2}, Va, O)_Q$$

This kind of model allows describing the composition variation from a metallic liquid, here (U, Am) to an oxide liquid (U, Am, O). To handle the metallic liquid, where only cations are present, hypothetical charged vacancies (Va) are included in the second sublattice. To extend to oxide systems, anions and neutral species are introduced. To ensure the electroneutrality, the number of sites on the

sublattices, *P* and *Q*, vary with the composition and they are equal to the average charge on the opposite sublattice:

$$P = \sum_j v_j y_{A_j} + Q_{y_{Va}}$$

$$Q = \sum_i v_i y_{C_i}$$

where y_i and v_i denote the site fraction and the charge of the constituent *i*, respectively (A for anion and C for cation).

In [19], the Gibbs energy of the liquid phase was not optimised for the ternary system and its description results purely from the extraction of the binary systems [2], [5], [21]. Thus, in this work, the ternary U-Am-O liquid phase has been assessed fitting the new experimental data and the resulting model is presented in section 4. The other phases of interest for this work, the $U_{1-y}Am_yO_{2\pm x}$ solid solution and the gas phase, were not modified and we refer to [19] for the description of their thermodynamic models.

3. Experimental results

3.1 Melting temperatures

The melting-T measurements were performed on the Am7, Am10, Am20, Am30 and Am50, both under argon and under air; for the Am70 sample, because of the limited quantity of material available, only measurements under air were performed. To prevent an excessive vaporization of the oxides, the autoclave was pressurized at 0.3 MPa.

A typical result of a melting measurement is reported in Figure 1. The laser-power profile is represented in black. One measurement was constituted by a pre-heating at about 1500 K, followed by four consecutive step-type laser pulses. These were programmed with different duration (100-200 ms) and intensity (for a maximum of 720 W), in order to exclude kinetic effects in the measured melting temperature. The red curve in Figure 1 is the thermogram (temperature vs time), acquired with the 655-nm pyrometer. The melting temperature is determined in two ways: first, from the cooling part of the thermogram, by locating the main thermal arrests; second, with the "reflected

light signal" (RLS) method, in which abrupt changes in the reflectivity of the sample indicate the change from the solid to the liquid phase. However, for solid solution such as $U_{1-y}Am_yO_{2\pm x}$, a non-congruent melting is expected and hence two thermal arrests should be observed during the cooling, corresponding to the *liquidus* and the *solidus* temperatures, respectively. In our measurements, only one thermal arrest was always clearly visible and, as shown in previous studies on similar materials [13], [22], this is associated to the *solidus* temperature T_m. Thus, in the following, we will always refer to the *solidus* temperature, except otherwise specified.

At the end of the measurement (four consecutive laser pulses), the sample was left to cool down to room temperature and checked by visual inspection. The autoclave windows were cleaned (vaporization of the sample) and the gas replenished. Then, the measurement was repeated several times in order to improve the result statistical analysis.
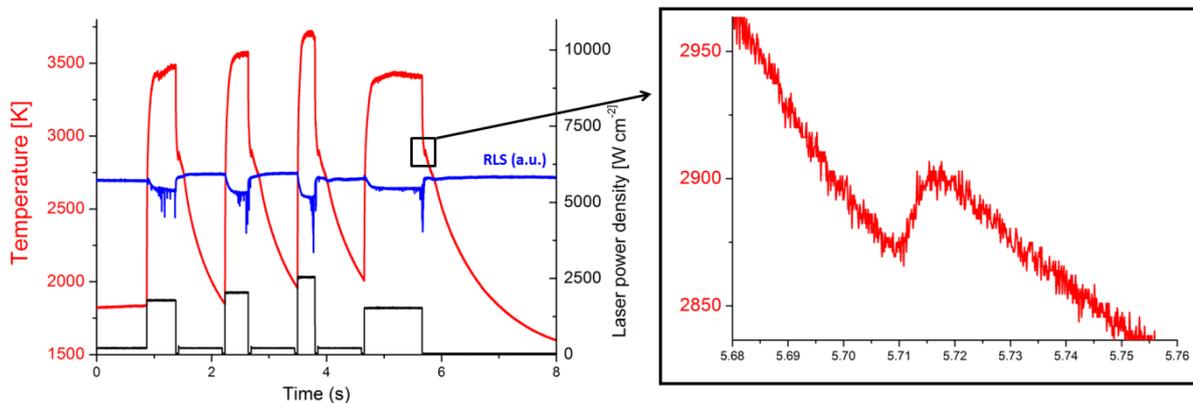

Figure 1. Thermogram (red), laser power profile (black) and reflected light signal (blue) recorded in a laser melting measurement in argon on the Am50 sample.

For the (U,Am)O_2 oxides with 0.07 ≤ Am/(Am+U) ≤ 0.48, several consecutive measurements of the melting temperature were performed, both under argon and air. For some of the compositions, more than one pellet (from the same batch) were used for the experiments (depending on the material availability). A general overview of all the obtained results is presented in Figure 2.

Error bars were omitted for visual clarity, but the uncertainty of each measurement was determined according to the error propagation law, taking into account the standard uncertainty associated to the pyrometer calibration (±10 K at 3000 K), the sample emissivity (±21 K at 3050 K) and the accuracy

in detecting the onset of vibrations in the RLS signal. The estimated cumulative uncertainty is ±2% of the reported temperature.
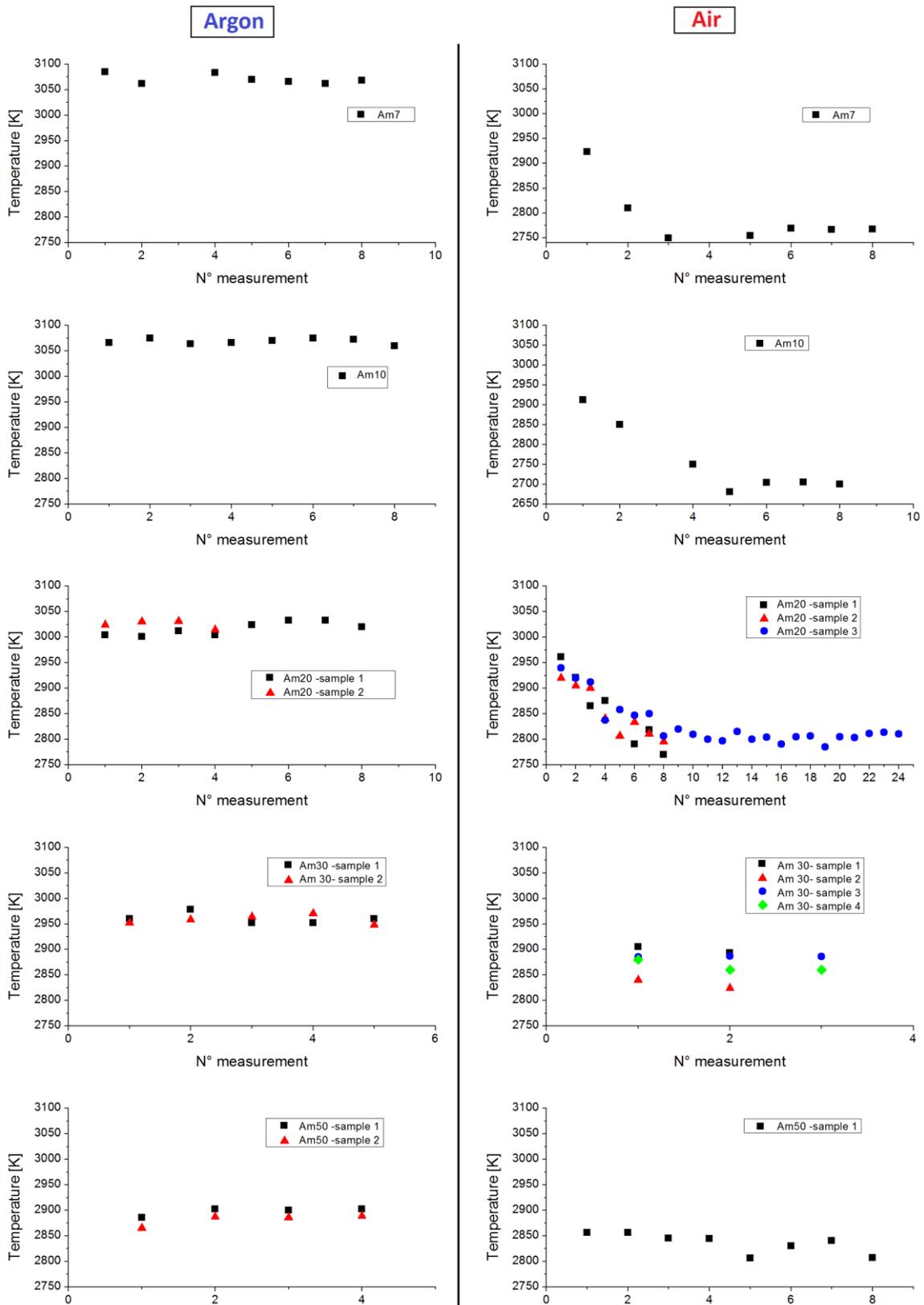

Figure 2. *Solidus* temperature results obtained in successive measurements in Ar and air.

Figure 2 shows that the $(U,Am)O_{2\pm x}$ oxides exhibit different behaviours under argon (left) and under air (right). For all the compositions, the measurements under argon were very reproducible. The obtained T_m values generally decrease with the americium content of the sample. A more complicated behaviour was observed under air. For the samples with $0.07 \leq Am/(Am+U) \leq 0.2$, the measured T_m decreased during the first laser shots and then it stabilized to 300-400 K lower values. For $Am/(Am+U) = 0.20$, three pellets were available for the experiment and this evolution was repeatable for all the samples. For the Am30 and Am50 samples, no clear evolution of the *solidus* temperature was observed during the attempts in air. The obtained values were close to those measured in argon, but slightly lower in any case.

For the $U_{0.33}Am_{0.67}O_{1.90}$ composition, only a small fragment of pellet was available for the experiment. and hence only one measurement under air could be performed.

The average values of the melting temperature measurements are represented as a function of the initial $Am/(Am+U)$ ratio in Figure 3. For the measurements under air, only the data obtained after the initial evolution were considered. For comparison, the literature data for UO_2 [23], AmO_{2-x} [3] and (U, Am)O_{2+x} oxides [6] are also reported in Figure 3.
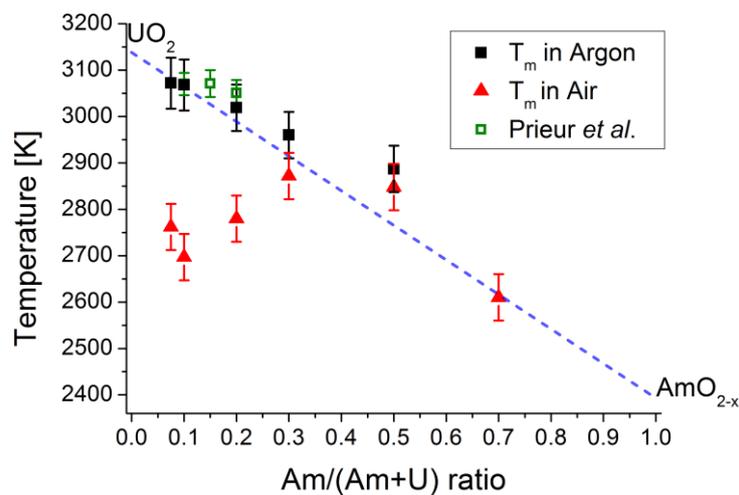

Figure 3. Melting (*solidus*) temperatures as a function of the initial Am/(Am+U) ratio of the samples. The results of this work are compared to the data reported in the literature for UO_2, AmO_{2-x} and (U, Am)O_2 oxides with Am/(Am+U)=0.10, 0.15, 0.20.

The *solidus* temperatures measured by Prieur *et al*. [6] under argon are in good agreement with the values observed in this work in the same atmosphere. A monotonic, almost linear decrease of the melting temperature with the Am/(Am+U) ratio is observed in this case. It is important to remember that the initial O/M ratio of the samples was not equal to 2.0 for all the compositions. Besides, the O/Am ratio corresponding to the melting of AmO_{2-x} is unknown. Therefore, the UO_2-AmO_{2-x} dashed line in Figure 3 was drawn as a guide to the eye only.

The melting temperatures measured under air are generally lower than those obtained under argon. The variation with the Am/(Am+U) ratio is not monotonic in this case. Close values, around 2700-2760 K, were observed for Am/(Am+U) = 0.07 and 0.10. These values are almost 400 K lower than those measured in argon. For 0.10 < Am/(Am+U) ≤ 0.48, an increase of the melting temperature with the americium content is observed. The highest values are found for the Am30 and Am50 samples. Interestingly, the values obtained for these two compositions under air and under argon are very close. Finally, a large decrease of the melting temperature was observed for Am/(Am+U) = 0.67 in air. The difference between the results obtained under argon and air clearly indicates a variation of the composition of the investigated samples. The clear evolution/decrease of the melting temperatures in air can be attributed to the O/M increase and, probably, the formation of hyper-stoichiometric oxides such as M_4O_9 and M_3O_8. Moreover, also changes of the Am/(Am+U) ratios cannot be excluded. Despite the overpressure imposed during the experiment, a partial vaporization of the sample could not be completely avoided. This was clearly observed during the experiments under air: at the end of each measurement series, the windows of the autoclave were covered in powder. Thus, the vaporization of the solid phase could also lead to variations of the Am/(Am+U) ratio.

In order to obtain reliable phase diagram data, post-melting characterizations were carried out.

3.2 Post-melting SEM

SEM microscopy images were obtained on the melted fragments, as those shown in Figure 4 for the Am50 sample melted in argon. The images confirm that only a small fraction of the pellet was melted during the measurement. Indeed, the more internal part in respect to the surface targeted with the

laser (region 3) maintained the microstructure usually observed in ceramic actinide dioxides, with well-faceted grains of about 10-20 μm. Moving toward the surface, an "intermediate region" appears (region 2), with round-shaped grains that start to connect each other. This part of the sample was at high temperature and it was about to melt.

Finally, the surface heated by the laser is clearly discernible in the fragment, because the initial microstructure with well-faceted grains is lost. The melted part seems more dense and compact, without grain boundaries. At higher magnification (region 1), columnar dendrites, typical of the solidification process, can be observed.

Figure 4 shows that the melted part is a small fraction of the sample, with a thickness of about 150-200 μm. Although this characteristic of the laser-heating technique is ideal for the study of high temperature property, the drawback is that the material available for the characterization is very limited. For this reason, the melted samples could only be investigated by XAS, since this technique demands only few mg of materials.
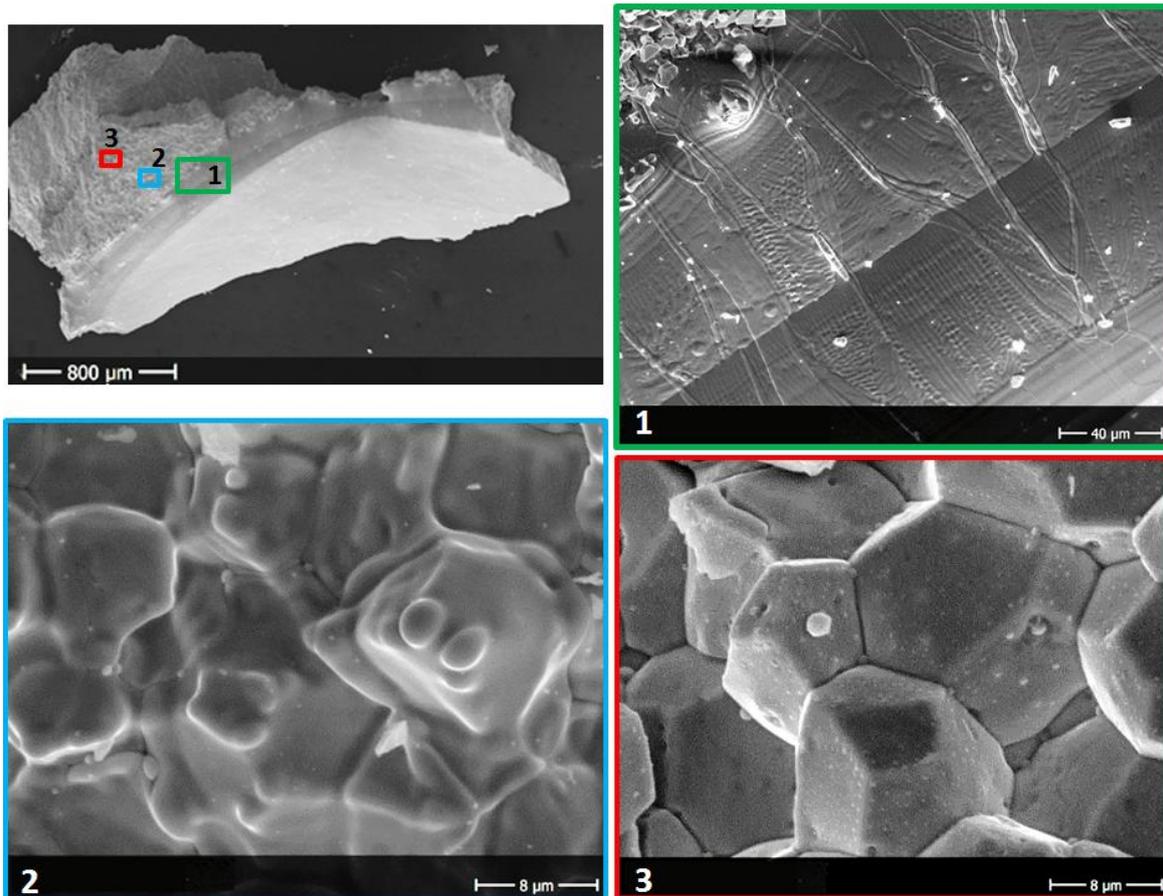
Figure 4. SEM images acquired on the Am50 sample melted in argon.

3.3 Am/M ratio by X-ray fluorescence spectroscopy

All the as-sintered and melted oxides were characterized by XAS, with the exception of the Am70 sample, which could not be retrieved after melting.

As explained in 2.4, for incident X-ray with energy equal to 18.9 keV (above both the U-L3 and Am-L3 edges), the ratios between the intensities of the fluorescence X-rays emitted by americium and uranium will be proportional to the ratio of their masses in the sample (Equation 3). As an example, one of the X-ray fluorescence spectrum acquired on the as-sintered Am20 sample is shown in Figure 5-(a). The two peaks observed at about 13614 eV and 14620 eV corresponds to the characteristic fluoresce X-rays emitted by uranium and americium, respectively. For all the as-sintered samples, the ratio between the intensity of these two fluorescent peaks was computed. For the intensity, both the maxima and the area of the peaks were tested. Besides, two different detectors were simultaneously

used for recording the fluorescence emission. For all the cases, the obtained $I_f(Am)/[I_f(Am) + I_f(U)]$ ratios were very similar. The values are represented as a function of the "real" (previously determined by TIMS) composition of the sample in Figure 5-(b). As expected, a linear trend was obtained:

$$\frac{I_f(Am)}{I_f(Am) + I_f(U)} = a \cdot \frac{Am}{Am + U} + b$$

Equation 4

The *a* and *b* parameters were obtained by fitting the points of Figure 5-(b).

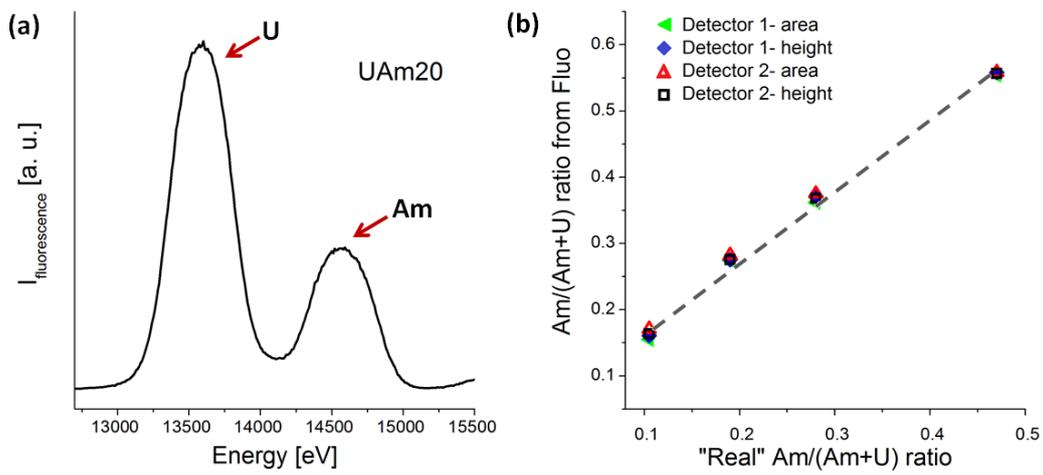**Figure 5. (a) Fluorescence X-ray spectrum of the Am20 sample for incident X-ray with E = 18.9 keV. (b) Am/(Am+U) ratio obtained by fluorescence spectroscopy for the as-sintered samples.**

The fluorescence spectra of the melted oxides are compared to the as-sintered samples in Figure 6. Small but clear differences in the $I_f(Am)/I_f(U)$ ratios between the melted and as-sintered samples are observable for the Am20, Am30 and Am50 oxides. A higher Am intensity is observed for all the melted samples, especially for those melted in air. The Am/(Am+U) ratios were determined by

inverting Equation 4 and the results are shown in Figure 6-bottom, right (see also Table 2 in Annex).
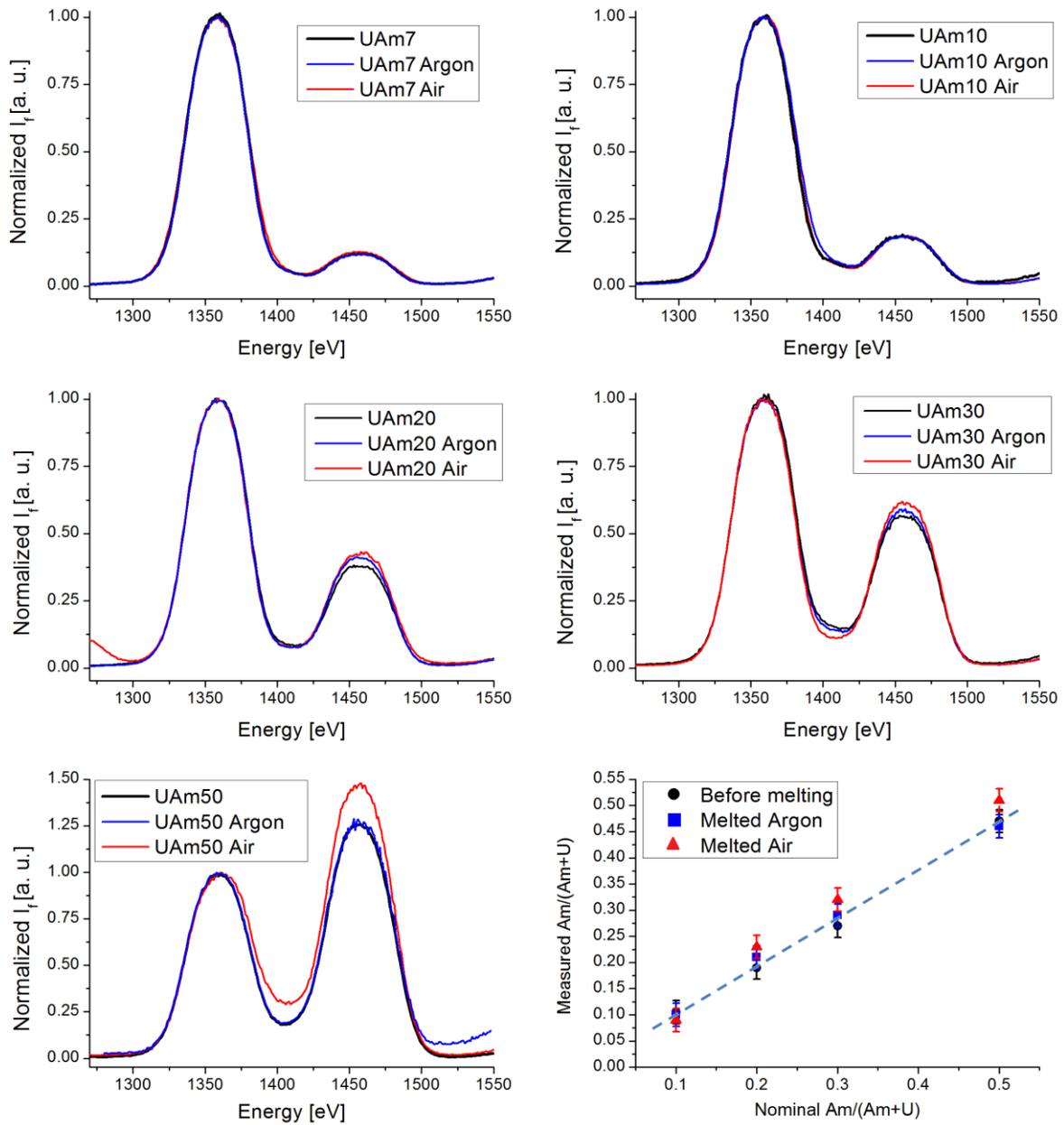

Figure 6. Comparison of the fluorescence spectra obtained on the as-sintered and melted samples of each composition and (bottom-right) resulting Am/M ratio vs the nominal Am/M.

The obtained Am/(Am+U) ratios of the melted samples are very close to the initial ones. This confirms that the rapidity of the laser-heating technique prevents important chemical composition changes. However, for the nominal compositions Am/(Am+U) = 0.2, 0.3 and 0.5, the results systematically show a slightly higher americium content (2-3 mol.%).

3.4 O/M ratio by XANES

The XANES spectra collected on the as-sintered as well as on the melted samples are show in Figure 7 and Figure 8, respectively for the Am-L_3 and U-L_3 edge. The white line positions are compared in the bottom-right of Figure 7 and Figure 8 (see also Table 3 in the Annex).
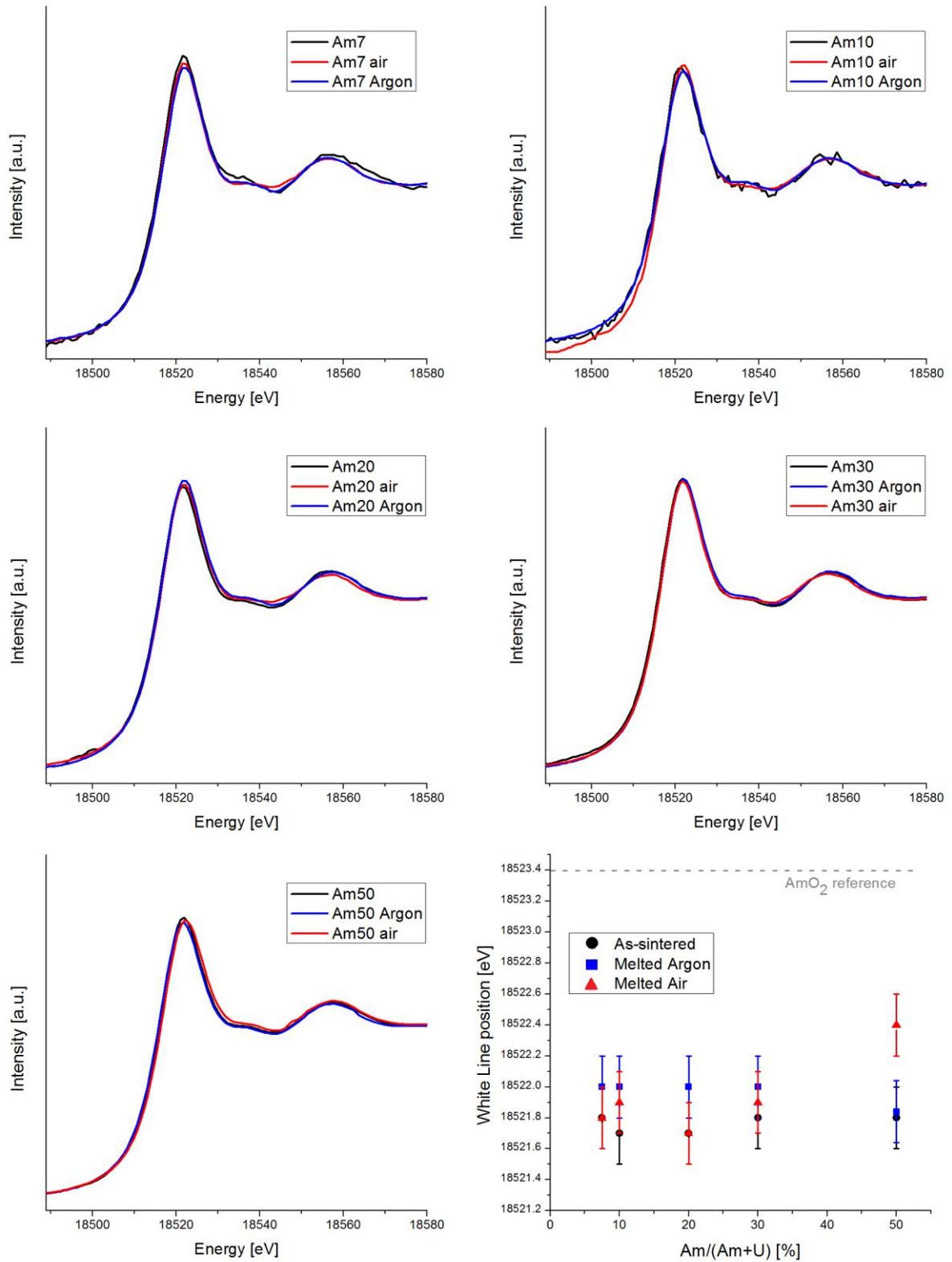
Figure 7. XANES spectra collected at the Am-L$_3$ edge of Am on (U,Am)O$_2$ oxides, before and after melting. Bottom right: observed white lines.
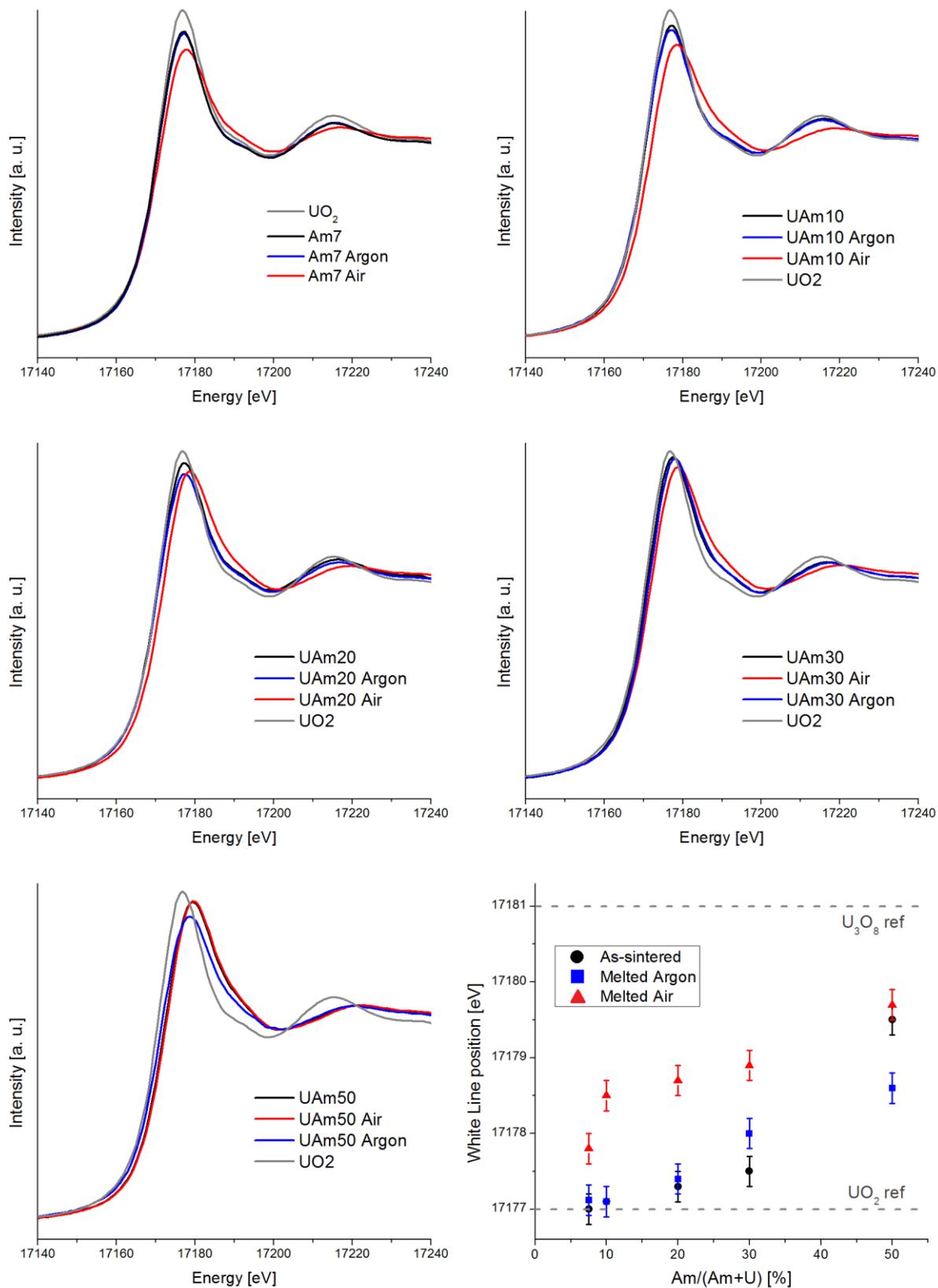
Figure 8. XANES spectra collected at the U-L$_3$ edge of Am on (U,Am)O$_2$ oxides, before and after melting. Bottom right: observed white lines.

For the Am-L_3 edge, the inflection point and white line positions of all the melted samples are identical, within the experimental uncertainty, to the as-manufactured oxides. In these latter, as shown in [10] and [24], americium is purely trivalent. Only for the Am50Air sample (melted in air), a small shift of the inflection point and the white line toward higher energies is observed. This indicates a slight oxidation of americium in this sample.

A more complicated picture is observed for the U-L_3 edge. For the as-sintered samples, the white line energies generally increase with the americium content, indicating a higher average oxidation state of uranium. This is consistent with the previous results reported in the literature [10], [24], [25]. For the oxides melted under argon, the white lines are very close to the corresponding as-sintered samples, for Am/(Am+U) ≤ 0.20. For Am30Argon, the white line is shifted to higher energy, indicating an increased oxidation. On the contrary, for Am50Argon, the white line is shifted to lower energy, pointing out a reduction. Finally, for the samples melted in air, the white lines are always shifted toward higher values, indicating an increase of the oxidation state of uranium.

The average oxidation state of uranium and americium were obtained by linear combination fit of the XANES spectra, using reference compounds. For the U-L_3 edge, $U^{4+}O_2$, $(U^{5+}_{2/3},U^{6+}_{1/3})_3O_8$ [26] and $Am^{3+}_{0.28}U^{4+}_{0.40}U^{5+}_{0.32}O_{2.02}$ [10] (the Am30 sample) were used as references, whereas $Am^{4+}O_2$ and a Am^{3+}-oxalate were adopted for the Am-L_3 edge. The results of the linear combination fits are detailed in the Annex (Table 4) and the obtained O/M ratios (computed using the measured Am/M values) are represented in Figure 9.
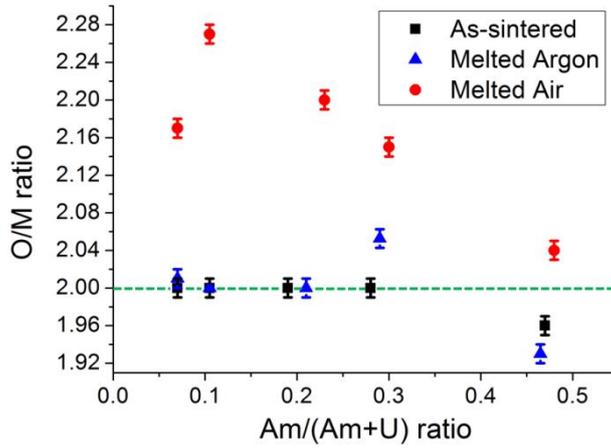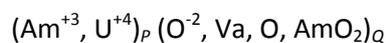
Figure 9. Composition of the melted samples obtained by XAS investigation.

For the as-sintered samples, the O/M values are identical (within the uncertainty) to those obtained in the previous investigation [10]. For the samples melted in argon, the oxygen stoichiometry was maintained for the compositions with Am/(Am+U) ≤ 0.20. For Am50Argon, the O/M ratios was lower than the initial ones. For Am30Argon, an oxidation is observed, from O/M = 2.02 to 2.05, which is quite surprising because this result is not consistent with the trend of the other compositions. Therefore, this result should be considered with caution because probably an alteration of the sample occurred during the storage or the preparation for the XAS measurements. Finally, an increase of the O/M ratio occurred for all the samples melted in air. The oxidation was particularly large for the oxides with low americium content, and especially for the Am10Air sample. In this case, an O/M = 2.28(2) was obtained and hence hyperstoichiometric oxide as M_4O_9 and M_3O_8 were surely formed, even if the identification of the phases could not be performed. The increase of the O/M ratio seems less and less important with the increasing of the Am/M ratio: the oxidation was very limited for the Am50Air sample, whose final O/M was equal to 2.04(2).

4. Thermodynamic modelling

The U-Am-O Calphad model proposed in [19] was here modified in order to reproduce the new *solidus* temperature data. First, the *AmO₂* species was added to the partially ionic 2-sublattice model [20] of the liquid phase, which became:

$$(Am^{+3}, U^{+4})_P (O^{-2}, Va, O, AmO_2)_Q$$

23

The choice of the constituents in the liquid sublattices is generally based on the assumption that the compounds showing a high stability in the solid state should be present in the liquid state. For the Am-O system, the highest melting points are exhibited by hexagonal-Am_2O_3 and AmO_2 [5], [27]. The first was already represented in the liquid state by Am^{3+} cations and O^{-2} anions. AmO_2 was here added as a neutral species based on the analogy with the similar Pu-O system modelling [2].

Since no data are reported for the enthalpy of melting of AmO_2, the value of UO_2 was adopted in first approximation (75 kJ/mol) [29]. Hence, by imposing the melting point of AmO_2 at 2386 K [27], an entropy of melting of 24,959 $J\cdot mol^{-1}\cdot K^{-1}$ was obtained. The following thermodynamic parameter was hence added to the Gibbs energy function of the liquid phase:

$$G_{AmO_2}^{liq} = GAMO2 + 61100 - 24.959 \cdot T$$

Where *GAMO2* is the Gibbs energy function of the solid stoichiometric AmO_2 reported in [19].

Moreover, a ternary interaction parameter between UO_2 and AmO_2, $L_{(U^{4+})(O^{2-},AmO_2)}^{liquid}$ was optimized by fitting the experimental *solidus* temperatures, as shown in Figure 10 (dashed lined). For the calculations, the total pressure was fixed to 0.3 MPa and the *solidus* temperature was computed as a function of the Am/(Am+U) ratio for $U_{1-y}Am_yO_{2\pm x}$ in equilibrium with the gas phase (argon or air). To reproduce the experiments under argon, the total composition of the system was set equal to 1 mole of metal (Am+U), 2 moles of oxygen and 5 moles of argon; to reproduce the experiments in air, 1 mole of metal, 3 moles of oxygen and 4 moles of nitrogen were considered. The choice of the number of gaseous moles (argon, nitrogen and oxygen) is quite arbitrary, because it is rather difficult to assess the actual mole ratio of the condensed and the gaseous species interacting during the laser-heating experiments. Nevertheless, the approach here adopted for the calculations is as close as possible to the experimental conditions, since the oxygen stoichiometry of the condensed phase was not fixed in the computation but left free to vary as a result of the interaction with the gas.
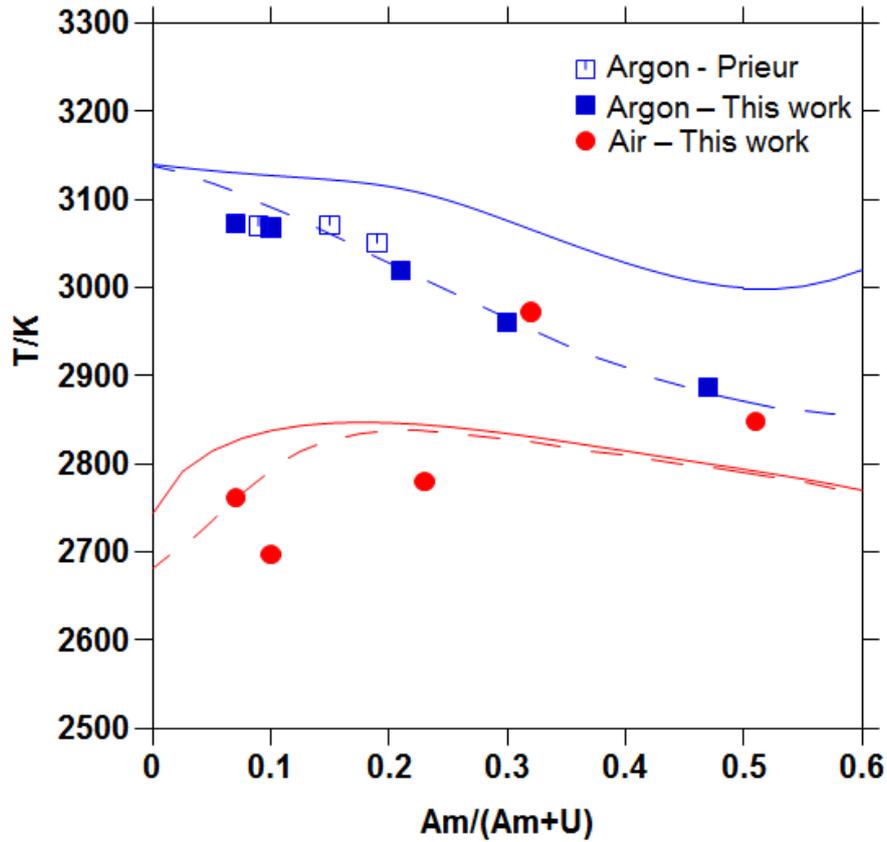
Figure 10. Computed solidus (- -) and liquidus (—) temperatures under argon (blue) and air (red), compared to the experimental points of Prieur [6] and this work.

A very good result, in particular for the solidus temperatures under argon, was obtained for an interaction $L^{liquid}_{(U^{4+})(O^{2-},AmO_2)}$ parameter equal to -680 kJ·mol^{-1}.

The *liquidus* temperatures were also calculated with the new model and represented in Figure 10 with solid lines. For the investigated composition range, the computations show that the *liquidus* is quite close to the *solidus*, with a maximum difference of about 100 K. This is consistent with the impossibility to observe the *liquidus* during the experiments, since previous studies have shown that the laser-flash technique can hardly discern the *solidus* and the *liquidus* in such cases because of the rapidity during the cooling [13], [22].

5. Discussion

The melting behaviour of $(U,Am)O_2$ oxides is dramatically affected by the oxygen partial pressure of the surrounding environment. Indeed, two different behaviours were observed for the experiments performed in this work under inert (argon) and oxidizing atmosphere (air). In the first case, the measurements were always repeatable, and the resulting melting temperatures decreased with the americium content of the sample, with a regular trend. On the contrary, under air, the measurements were not reproducible for the oxides with Am/(Am+U) ≤ 0.20. In these cases, the observed melting temperature decreased during the first attempts and then it stabilized at about 400 K lower values. Based on this behaviour, it was clear that the composition of the oxide varied during the measurements in air, likely because of an increase of the O/M ratio, whereas a mostly constant composition could be supposed for the measurements in argon. These hypotheses were checked performing post-melting characterizations, by determining the Am/(Am+U) and O/M ratios of the melted samples by X-ray fluorescence spectroscopy and XANES, respectively.

The variations of the Am/(Am+U) ratios were limited, as expected considering the rapidity of the laser-heating technique. However, slightly higher Am/(Am+U) ratios were systematically observed for the melted samples, especially for those measured in air. This indicates that, in the Am/(Am+U) ≤ 0.48 domain, the vapor pressures of the uranium gaseous species are higher than those of americium, leading to a preferential vaporization of uranium, in agreement with the partial vapour pressures recently measured by Epifano *et al*. [19].

The changes of the O/M ratios during the laser-heating measurements were instead very important. The variations were particularly evident for the samples melted in air, for which a systematically increase of the O/M ratio was observed. The O/M changes were less important for the oxides melted in argon. For Am/(Am+U) ≤ 0.30, the initial and final O/M were equal, within the experimental uncertainty. A reduction was observed for the Am50Argon sample, whose initial O/M = 1.96(2) passed to O/M = 1.93(2). This is not surprising, since [10], [24] showed that the addition of americium in the fluorite structure generally stabilizes the hypostoichiometric domain.

The effect of the composition on the melting temperature is evident in Figure 11 (see also table in Annex), where the melting temperatures are plotted as a function of the final O/M and Am/M ratios.
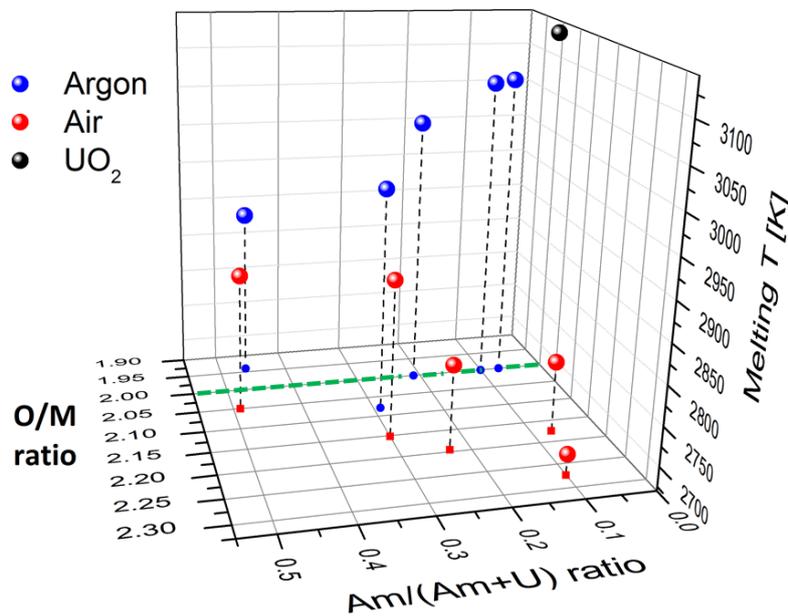

Figure 11. Melting temperature versus the final (room temperature) O/M-Am/M compositions.

The blue points in Figure 11 correspond to the measurements in argon. These points are close to the oxygen stoichiometry O/M = 2.00 and they show a regular decreasing trend with the increase of the americium content. The red points, corresponding to the melting temperatures observed in air, are generally lower than those in Argon, but the trend with the Am/(Am+U) ratio is opposite. The cause of this difference can clearly be attributed to the O/M ratios. Indeed, a consistent O/M increase was observed for Am/M ≤ 0.2, whereas it was more limited for Am/M = 0.30 and 0.50, confirming once again that the resistance toward the oxidation improves with the increasing americium content [19]. The increase of the O/M ratio has dramatic effects on the melting temperature, causing a 300-400 K decrease. This is clear looking to the Am10air sample: at the highest O/M ratio (2.28(2)) corresponds the lowest melting temperature (2697 ± 35 K).

Considering the composition changing during the laser-flash measurements, one can wonder whether the composition of the melted samples determined at room temperature is representative of the composition at the melting point, or if the O/M ratio evolves also during the cooling, even

after re-solidification. To have some insight on this subject, the Calphad model here optimized was used to compute the solidification paths of the two extreme compositions for which the final O/M has been measured: Am7 and Am50. The same computation strategy described in section 4 was here adopted to simulate argon and air atmospheres. The results are shown in Figure 12, in a temperature vs O/M graph, with the stable phase in each domain explicated in the legend. The rectangular orange areas on the graphs represent the experimental data: the rectangular base is centred on the O/M ratio measured after the melting, the width is the relative experimental uncertainty and the height is equal to the measured *solidus* temperature. An area has been traced instead of a single point to highlight the uncertainty on the temperature corresponding to the post-melting composition.
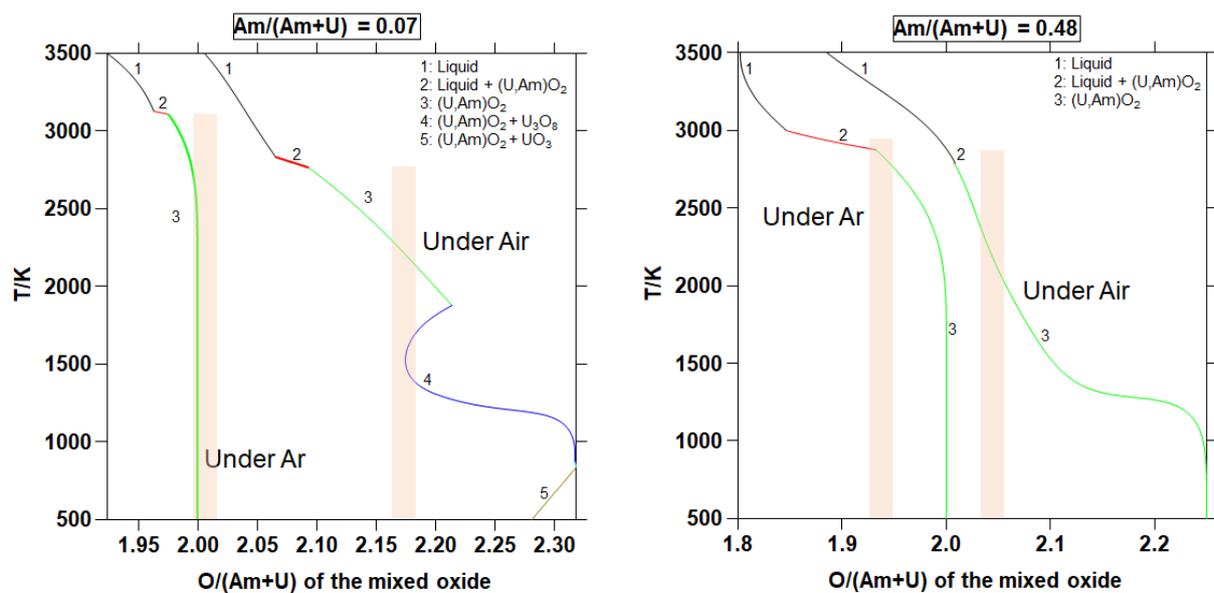

Figure 12. Cooling paths in a temperature-O/M ratio graph. The stable phases in each domain are specified on the figure. The orange rectangular areas are centred on the O/M ratio determined experimentally (at room temperature).

All the computed *solidus* temperatures (intersection between the parts 2 and 3 of the curve) are really close to the experimental values, showing again that a good fit of these data was obtained. Concerning the composition variation, the calculations show that an oxidation occurs along the cooling paths, as expected. More specifically, according to the model, the O/M ratio is not constant from the *solidus* point to room temperature: a further oxidation is expected also in the solid phase. Under argon, the stoichiometry O/M = 2 is reached at ≈2700 K and ≈2400 K, respectively for Am7 and

Am50, and this value is then stable till room temperature. Comparing the calculations to the experiments, a very good agreement is observed for Am50Argon, where the final O/M is equal to the composition of the *solidus* point (at 2848 K), whereas a re-oxidation occurs for Am7Argon during the cooling. Interestingly, for the latter, the O/M = 2 is reached around 2700 K. From these results, one can hence suppose that, in the O/M< 2 domain and for temperatures above 2700-2800 K, the diffusion of the oxygen is fast enough to induce composition variations in the solid phase.

For the experiments in air, the calculations show a continuous increase of the O/M ratio during the entire cooling, leading also to the formation of oxides richer in oxygen for Am7Air. For Am7Air and Am50Air, the O/M ratios determined experimentally intersect the calculated path at an intermediate point between the *solidus* and the room temperature. In both cases, this point corresponds to a temperature around 2300-2400 K. Thus, the variations of the O/M ratios occur also in the solid phase, likely in the temperature range T > 2300 K.

In conclusion, the comparison between the thermodynamic calculations and the compositions of the melted samples show that the laser-flash technique is fast enough to avoid the complete re-oxidation of the samples, but not enough to avoid slight increases of the O/M ratio at high temperature.

6. Conclusions

In this work, the laser-heating technique was used to investigate the melting behaviour of the $(U,Am)O_{2\pm x}$ solid solution over a wide composition domain, for Am/(Am+U) ratios ranging from 7 to 70 mol.%. Two different atmospheres (argon and air), were used for the experiments and this allowed to show the dramatic effects of the oxygen stoichiometry on the melting points. Thanks to accurate post-melting characterizations by XAS technique, the final compositions of the melted samples were determined. For the measurements performed in argon, O/M ratios close to 2.0 (or slightly lower) were generally maintained and, in this case, an almost linear decrease of the melting point was observed with the increase of the americium content, passing from 3072(55) K for Am7 to

2887 K for Am50. However, our study shows that the most dramatic effect on the melting point is related to the oxygen hyperstoichiometry: in the measurements in air, the O/M ratios increased, causing drops of the melting temperature up to almost 400 K. The oxidation and the related decrease in the melting temperature were more dramatic for the oxides richer in uranium, whereas they were hindered in the Am-rich samples by the high content of Am^{3+}. This effect is consistent with the previous similar results on $(U,Pu)O_{2+x}$ oxides [28], but the resistance against the oxidation is even more evident in the americium-doped oxides. Finally, the new experimental data of the *solidus* temperatures were used to improve the Calphad modelling of the U-Am-O system, optimizing the Gibbs energy of the liquid phase. For this assessment, an approach as close as possible to the experimental conditions was applied, simulating the interaction between the condensed and the gas phase, letting the O/M ratio free to vary. The obtained model was then used to better understand the laser-heating experiments, by tracing some solidifications paths for selected compositions. The results confirm that under argon, the oxygen to metal ratio is below 2 at the solidus temperature and that the samples are oxidized under air with O/M ratio higher than 2 for uranium rich samples. Thus the compositions determined at room temperature after the melting must be cautiously considered because, despite the rapidity of the experiments, variations of the O/M can occur during the cooling, also after re-solidification.

References

[1] E. D'Agata *et al.*, 'MARIOS: Irradiation of UO2 containing 15% americium at well defined temperature', *Nucl. Eng. Des.*, vol. 242, pp. 413–419, 2012.

[2] C. Guéneau *et al.*, 'Thermodynamic modelling of advanced oxide and carbide nuclear fuels: Description of the U–Pu–O–C systems', *J. Nucl. Mater.*, vol. 419, no. 1–3, pp. 145–167, 2011.

[3] R. E. McHenry, 'Melting Points of Curium and Americium Oxides', *Trans Am Nucl Soc 8*, p. 75, 1965.

[4] P. Gotcu-Freis, J.-Y. Colle, C. Guéneau, N. Dupin, B. Sundman, and R. J. M. Konings, 'A thermodynamic study of the Pu–Am–O system', *J. Nucl. Mater.*, vol. 414, no. 3, pp. 408–421, 2011.

[5] E. Epifano *et al.*, 'Insight into the Am–O Phase Equilibria: A Thermodynamic Study Coupling High-Temperature XRD and CALPHAD Modeling', *Inorg. Chem.*, vol. 56, no. 13, pp. 7416–7432, Jul. 2017.

[6] D. Prieur *et al.*, 'Melting behaviour of americium-doped uranium dioxide', *J. Chem. Thermodyn.*, vol. 97, pp. 244–252, 2016.

[7] T. Delahaye, F. Lebreton, D. Horlait, N. Herlet, and P. Dehaudt, 'Application of the UMACS process to highly dense U1–xAmxO2±δ MABB fuel fabrication for the DIAMINO irradiation', *J. Nucl. Mater.*, vol. 432, no. 1, pp. 305–312, Jan. 2013.

[8] F. Lebreton *et al.*, 'Recent progress on minor-actinide-bearing oxide fuel fabrication at CEA Marcoule', *J. Nucl. Mater.*, vol. 438, no. 1–3, pp. 99–107, 2013.

[9] F. Lebreton and F. Lebreton, *PhD thesis- Synthèse et caractérisation d'oxydes mixtes d'uranium et d'américium*. Limoges, 2014.

[10] E. Epifano et al., 'Unique features in the (U,Am)O2 solid solution', *Prep.*

[11] D. Manara, M. Sheindlin, W. Heinz, and C. Ronchi, 'New techniques for high-temperature melting measurements in volatile refractory materials via laser surface heating', *Rev. Sci. Instrum.*, vol. 79, no. 11, p. 113901, 2008.

[12] F. De Bruycker, K. Boboridis, P. Pöml, R. Eloirdi, R. J. M. Konings, and D. Manara, 'The melting behaviour of plutonium dioxide: A laser-heating study', *J. Nucl. Mater.*, vol. 416, no. 1–2, pp. 166–172, 2011.

[13] F. De Bruycker *et al.*, 'On the melting behaviour of uranium/plutonium mixed dioxides with high-Pu content: A laser heating study', *J. Nucl. Mater.*, vol. 419, no. 1–3, pp. 186–193, 2011.

[14] D. P. DeWitt and J. C. Richmond, 'Thermal Radiative Properties of Materials', in *Theory and Practice of Radiation Thermometry*, Wiley-Blackwell, 2007, pp. 91–187.

[15] C. M. Herzfeld and D. E. McFeron, 'Temperature: Its Measurement and Control in Science and Industry, Volume 3', *Phys. Today*, vol. 17, no. 3, p. 63, Jan. 2009.

[16] Y. Lu, Y. Yang, F. Zheng, B.-T. Wang, and P. Zhang, 'Electronic, mechanical, and thermodynamic properties of americium dioxide', *ArXiv12110378 Cond-Mat*, Nov. 2012.

[17] J. Rothe *et al.*, 'The INE-Beamline for actinide science at ANKA', *Rev. Sci. Instrum.*, vol. 83, no. 4, p. 043105, Apr. 2012.

[18] B. Ravel and M. Newville, 'ATHENA, ARTEMIS, HEPHAESTUS: data analysis for X-ray absorption spectroscopy using IFEFFIT', *J Synchrotron Radiat*, vol. 12, no. 4, pp. 537–541, 2005.

[19] E. Epifano, 'Study of the U-Am-O ternary phase diagram', thesis, Paris Saclay, 2017.

[20] B. S. H. LuKas S. G. Freis, *Computational Thermodynamics The Calphad Method*. 2007.

[21] M. Kurata, 'Thermodynamic database on U-Pu-Zr-Np-Am-Fe alloy system II — Evaluation of Np, Am, and Fe containing systems-', *IOP Conf Ser Mater Sci Eng*, vol. 9, no. 1, p. 012023, 2010.

[22] R. Böhler *et al.*, 'Recent advances in the study of the UO2–PuO2 phase diagram at high temperatures', *J. Nucl. Mater.*, vol. 448, no. 1, pp. 330–339, 2014.

[23] D. Manara, C. Ronchi, M. Sheindlin, M. Lewis, and M. Brykin, 'Melting of stoichiometric and hyperstoichiometric uranium dioxide', *J. Nucl. Mater.*, vol. 342, no. 1, pp. 148–163, Jun. 2005.

[24] F. Lebreton *et al.*, 'Peculiar Behavior of (U,Am)O2−δ Compounds for High Americium Contents Evidenced by XRD, XAS, and Raman Spectroscopy', *Inorg. Chem.*, vol. 54, no. 20, pp. 9749–9760, Oct. 2015.

[25] D. Prieur *et al.*, 'Local Structure and Charge Distribution in Mixed Uranium–Americium Oxides: Effects of Oxygen Potential and Am Content', *Inorg. Chem.*, vol. 50, no. 24, pp. 12437–12445, Dec. 2011.

[26] K. O. Kvashnina, S. M. Butorin, P. Martin, and P. Glatzel, 'Chemical State of Complex Uranium Oxides', *Phys. Rev. Lett.*, vol. 111, no. 25, p. 253002, Dec. 2013.

[27] R. E. McHenry, 'Melting Points of Curium and Americium Oxides', *Trans Am Nucl Soc 8*, p. 75, 1965.

[28] M. Strach, D. Manara, R. C. Belin, and J. Rogez, 'Melting behavior of mixed U–Pu oxides under oxidizing conditions', *Nucl. Instrum. Methods Phys. Res. Sect. B Beam Interact. Mater. At.*, vol. 374, no. Supplement C, pp. 125–128, 2016.

[29] R. J. M. Konings, et al., 'The Thermodynamic Properties of the f-Elements and their Compounds. Part2. The Lanthanide and Actinide Oxides', *Journal of Physical and Chemical Reference Data*, vol.43, 013101, 2014.

Acknowledgements

ANNEX

	Am/(Am+U) ratios (%)		
Sample	As sintered	Melted Argon	Melted Air
Am7	7.0(5)	7(1)	7(1)
Am10	10(1)	10(2)	10(2)
Am20	19(2)	21(3)	23(3)
Am30	28(2)	30(3)	32(3)
Am50	48(1)	47(1)	51(3)

Table 2. Am/(Am+U) ratios before and after melting, as obtained by X-ray fluorescence spectroscopy.

Sample	Am-L$_3$ edge (eV)		U-L$_3$ edge (eV)	
	E$_0$	WL	E$_0$	WL
Am7	18517.4	18521.8	17170.3	17177
Am7 Argon	18517.5	18522	17170	17177.12
Am7 Air	18516.9	18521.8	17171	17177.8
Am10	18517.1	18521.7	17170.2	17177.1
Am10 Argon	18517.1	18522	17169.8	17177.1
Am10 Air	18517.4	18521.9	17172.5	17178.5
Am20	18516.9	18521.6	17171.1	17177.5
Am20 Argon	18516.8	18522	17170	17177.4
Am20 Air	18517	18522.1	17172.8	17178.7
Am30	18516.9	18521.8	17171.5	17177.5
Am30 Argon	18517	18522	17172.4	17178
Am30 Air	18517	18521.9	17172.6	17178.9
Am50	18516.9	18521.8	17172.7	17179.5
Am50 Argon	18516.7	18521.8	17171.1	17178.6
Am50 Air	18517.3	18522.4	17173	17179.7
AmO$_2$	18518.9	18523.4		
UO$_2$			17170.3	17177
U$_3$O$_8$			17173.3	17181.1

Table 3. Energy positions of the inflection points and white lines of the XANES spectra presented. Values are given with a 0.3 eV uncertainty.

	Am-L$_3$ edge			U-L$_3$ edge				
Sample	Am^{3+}-ref	AmO$_2$	AOS	UO$_2$	Am30	U$_3$O$_8$	AOS	O/M
Am7	1	0	3	0.85	0.15	0	4.07	2.00(2)
Am7Argon	1	0	3	0.77	0.23	0	4.10	2.01(2)
Am7Air	1	0	3	0.66	0	0.34	4.45	2.17(2)
Am10	1	0	3	0.74	0.26	0	4.12	2.00(2)
Am10Argon	1	0	3	0.73	0.27	0	4.12	2.00(2)
Am10Air	1	0	3	0.28	0.26	0.46	4.74	2.28(2)
Am20	1	0	3	0.43	0.57	0	4.26	2.01(2)
Am20Argon	1	0	3	0.80	0	0.20	4.27	2.00(2)
Am20Air	1	0	3	0	0.58	0.42	4.82	2.20(2)
Am30Argon	1	0	3	0	0.87	0.13	4.57	2.05(2)
Am30Air	1	0	3	0	0.59	0.41	4.82	2.12(2)
Am50	1	0	3	0	0.69	0.31	4.75	1.96
Am50Argon	1	0	3	0.43	0.14	0.43	4.62	1.93
Am50Air	0.67	0.33	3.33	0	0.54	0.46	4.85	2.04(2)

Table 4. Results of the linear combination fit of the U-L$_3$ and Am-L$_3$ XANES spectra.

Measurements in Argon		
Am/(Am+U) ratio (%)	O/M ratio	T$_m$ (K)
7(1)	2.01(2)	3072(55)
10(2)	2.00(2)	3068(55)
21(3)	2.00(2)	3019(50)
30(3)	2.05(2)	2960(50)

47(3)	1.93(2)	2887(50)
Measurement in Air		
7(1)	2.17(2)	2762(50)
10(2)	2.28(2)	2697(50)
23(3)	2.20(2)	2780(50)
32(3)	2.12(2)	2972(50)
51(3)	2.04(2)	2848(50)

Table 5. Melting temperatures and final compositions obtained at room temperature by post-melting characterisation.